PNAS
www.pnas.org

Supplementary Information for

Amorphous Polymer Dynamics and Free Volume Element Size Distributions from Ultrafast IR Spectroscopy

David J. Hoffman, Sebastian M. Fica-Contreras, and Michael D. Fayer

Department of Chemistry
Stanford University, Stanford, CA 94305

*Michael D. Fayer
Phone: 650 723-4446; Email: fayer@stanford.edu

This PDF file includes:

Supplementary text
Figures S1 to S6
Tables S1 to S4
SI References

Isotropic Heating Signal

In addition to the population dynamics, the isotropic signal additionally reveals that there is a heating signal in the pump-probe spectra at long waiting times. It was determined that this arises from background absorption of the polymer creating local heating effects. The local heating induced by the pump pulse causes an extremely small frequency shift in the absorption spectrum of the PhSeCN stretch which in turn causes a difference signal to appear at long waiting times. The heat signal grows in over the course of about 10 ps, after which it is essentially static. The heating was found to be isotropic, which means that the numerator of the anisotropy ($r(t)$, Eq. 3) is unaffected. However, as the denominator contains the isotropic component, it is necessary to address the heating to avoid artifacts in the anisotropy.

The heating was addressed using two techniques. First it was partially suppressed experimentally through AOM pulse shaping. Instead of completely blocking the pump during the "off" shot, the AOM blocked only the frequency components corresponding to the CN stretch. As the laser bandwidth (~100 cm^{-1} FWHM) is much broader than the CN absorption (~10 cm^{-1} FWHM), most of the pulse energy remained during the "off" shot. This pulse shape maintained much of the polymer heating during the "off" shots and reduced the heat signal by ~60%. The remaining heat signal, which was only large compared to the desired nonlinear signal at very long waiting times, was removed by performing a time independent, frequency dependent subtraction of the long-time heating signal. The subtracted value was determined by fitting every frequency dependent isotropic signal to an exponential decay to an offset. By sharing the decay constant across the entire band and floating the amplitude and offset, the frequency dependent heat offset was determined. Employing this correction enabled accurate determination of the anisotropic decay.

Transition Frequency Stability and 2D IR Spectroscopy

For the frequency dependent anisotropy decays to occur, the transition frequencies of probe molecules must be essentially constant over the experimental timescale. If the frequencies of the vibrational probes within the inhomogeneous

spectrum were able to randomize on a timescale short or comparable to the experiment, then a probe's dynamics would not be associated with a well-defined frequency (structural environment). In other words, to see differences in the pump-probe anisotropic decays with frequency, there must be persistent correlation in the frequency between when the pump pulse excites the sample and when the probe pulse reads out the information at a time *t* later. The correlation between the initial frequency and the frequency after a given delay time (waiting time) can be measured quantitatively with 2D IR spectroscopy (1, 2).

The details of the 2D IR experiment have been presented previously (1-3). Qualitatively, the 2D IR experiment creates a 2D correlation plot between the initial frequency and final frequency of a vibrational transition after a given waiting time, T_w. The degree of correlation at a given T_w is dependent on the rate of "spectral diffusion," or the rate at which the instantaneous frequency of the probe molecule diffuses throughout the inhomogeneous absorption spectrum due to changes in the probe molecule's environment. If the waiting time is short compared to the timescale of spectral diffusion, then the 2D spectrum will appear elongated along the diagonal, indicating a high degree of correlation between the initial and final frequencies. If the waiting time is much longer than the timescale of spectral diffusion, then the 2D spectrum will appear round instead. The degree of correlation can be made explicit through the frequency-frequency correlation function (FFCF): $C(T_w) = \langle \delta\omega(0)\delta\omega(T_w) \rangle$, where $\delta\omega$ is the instantaneous vibrational transition frequency. The normalized FFCF can be extracted from the 2D spectrum with the Center Line Slope (CLS) method (4, 5). The CLS is calculated by taking slices of the 2D spectrum along one frequency axis and finding the maximum of each slice. The maxima are then fit to a line, and the slope of the line corresponds to the normalized frequency-frequency correlation function for that waiting time.

Like the pump-probe intensities, the value of the FFCF can be polarization dependent (6, 7). A polarization dependence can arise because there can be two sources of spectral diffusion: "structural spectral diffusion" (SSD) that arises from the structural evolution of the chemical system, and "reorientation-induced spectral diffusion" (RISD) that arises specifically from the motion of the vibrational probe in a vector potential. For comparison to the pump-probe anisotropies in systems with substantial polarization

dependence, the 2D spectra that were acquired in the perpendicular polarization were subtracted from the corresponding parallel polarization spectra. The CLS was then obtained for the constructed anisotropic spectra.

Anisotropic 2D spectra for a short (1 ps) and long (200 ps) T_w are shown in Fig. S1 (inset). Although there is some degree of decorrelation on these experimental timescales, the 2D spectra remain highly correlated for both waiting periods. Fig. S1 displays the anisotropic CLS decay for the experimental time window. The data show that over the entire experimental time range, the value of the CLS remains above 0.7. This is a highly correlated line shape. The 2D IR experimental results show that the frequencies of a subensemble of molecules change somewhat but demonstrate that the vibrational frequencies are stable enough to permit the observation of frequency dependent orientational dynamics as displayed in Figs. 1 and 2. Detailed analysis of the 2D spectra shows that at the longest times, the tails of the distribution of expanded frequency ranges overlap with each other to some extent, but the overlaps are sufficiently small that orientational dynamics measured at the different wavelengths can be clearly distinguished, which is what is observed.

The short time decay of spectral diffusion shown in Fig. S1 (approximately 10 ps) coincides with the time scale of angular motions in the first diffusive cone. The similarities in time scales may be indicative of the time required for structural constraint release that is necessary within the wobbling-in-a-cone model for additional orientational relaxation of the PhSeCN probe molecules to occur, i.e., the second diffusion cone. The fast structural dynamics can occur through motions of side groups or small density fluctuations.

The corresponding 2D IR measurements on the PMMA oligomer confirm this picture. Fig. S2B shows the anisotropic CLS decay at 260 K and the parallel CLS decay at 360 K. The parallel CLS for 360 K is shown, as the polarization dependence was minimal and the 2D anisotropic spectra were low amplitude. At low temperature, the CLS decays to a small extent showing that the frequencies remain highly correlated over the experimental time window, similar to the high MW PMMA data. By contrast, the high temperature data loses correlation very quickly. The CLS decays to zero. A CLS value of zero means that all probe molecules have sampled all frequencies, and therefore

all oligomer structures that give rise to the inhomogeneously broadened absorption spectrum. These observations confirm the relationship between the slow spectral diffusion (slow polymer structural dynamics) and the frequency dependent anisotropy proposed in the previous section.

Wobbling-in-a-Cone Total Orientational Relaxation Diffusion Constants

If a system can undergo complete orientational relaxation, the parameterization in Eq. 4 of the main text is modified with an additional exponential term (8):

$$C_2(t) = S_0^2\left(S_1^2 + \left(1-S_1^2\right)\exp(-t/\tau_1)\right) \times\left(S_2^2 + \left(1-S_2^2\right)\exp(-t/\tau_2)\right)\exp(-t/\tau_{or}) \quad \text{(S1)}$$

where τ_{or} is the time scale of complete orientational randomization. This is the case in the low Mw PMMA at 360 K (see Table S3).

The wobbling-in-a-cone model also enables the time constants (τ_1 and τ_2 in Eq. 4 and Eq. S1, Table S1-S3) measured by the PSPP experiments to be associated with an angular diffusion constant. For small to moderate cone angles θ_i, the measured time constant τ_i can be related to the orientational diffusion constant (D_i) in the cone by (9):

$$\tau_i = 7\theta_i^2/24D_i \quad \text{(S2)}$$

where θ_i is the cone angle in radians. While the measured time constants are essentially constant across the absorption band, the cone angles change substantially. The change in cone angles results in orientational diffusion in the smaller cones to be slower, which can be understood qualitatively as the molecule needing the same amount of time to sample a smaller range of angles.

DFT Calculations of PhSeCN for use in the ROAM model

DFT calculations were performed on PhSeCN to determine the center of mass of the molecule after structural optimization and to determine how freely the phenyl ring can rotate. All DFT calculations were performed using B3LYP and the 6-31G(d,p) basis set.

The center of mass of a structurally optimized PhSeCN can be seen in Fig. S3A (intersection of the axes). The center of mass lies approximately along the Se-C bond that

connects the SeCN to the phenyl ring. Depending on the conformation of the ring, the center lies approximately 1.4 Å away from the Se atom, and the most distant atom from the center of mass is the para-hydrogen atom, which is about 4.3 Å away. The center of benzene ring can also be calculated and was found to be about 2.0 Å away. These numbers were used in the ROAM models presented in the main text.

It was also of interest to see the barrier to rotation of the C-Se bond connecting the phenyl ring and the SeCN moiety. By calculating the energy of the molecule at a range of dihedral angles, the barrier to rotation was found to be 1.38 kcal/mol in the gas phase (Fig. S3B). This low barrier indicates that the rotation of the C-Se bond could play a role in setting the range of angles that are accessible to the PhSeCN molecule in a given free volume element.

Comparison to the Other Experimental Measures of Free Volume

The main text discussed the comparison of the ROAM FVE measures to the FVE measures predicted by PALS. Here the results of the photoisomerization method and SAXS in PMMA are compared to ROAM and PALS.

The photoisomerization method works by placing different molecules (generally stilbene or azobenzene derivatives) into the polymer (10, 11). When an embedded molecule is excited electronically, it attempts to undergo a structural isomerization, but it can only succeed in structurally rearranging if there is sufficient free volume for the transformation to occur. The fraction of the embedded molecules that isomerize is thought to be determined by the fraction of free volume that is large enough for the reaction to occur. By repeating the experiment for photoisomerizable molecules of different sizes, a distribution of free volume size is reported. Notably the free volume distribution predicted by this method is consistently larger than measured by PALS or other common techniques, such as ^{129}Xe-NMR (12-14). At room temperature for unaged PMMA, the modal FVE was found to have a radius of 4.5 Å (11), nearly twice as large as the PALS measurement. The discrepancy has been associated with the large size of photoisomerizable molecules (even the smallest are nearly twice as large as the PhSeCN molecule) biasing the measurement to larger sites or creating larger elements than would typically occur (12). It is also worth noting that while the isomerization reactions occur

on nanosecond timescales, the samples are irradiated for minutes to achieve a photoequilibrium (10). This is in contrast to PALS and ROAM, which make the measurements on a short timescale.

In addition to the PALS and photoisomerization techniques, an average FVE size has been estimated based on small-angle x-ray scattering (SAXS) results. The SAXS result was found to be consistent with FVEs of average size between 3 and 5 Å (15). Due to the low precision of the technique it will not be considered further.

A complete comparison of the photoisomerization and SAXS results to the ROAM and PALS results can be found in Fig. S4. The cumulative distribution obtained from the total cones (red circles, Fig. S4A and S4B) occurs somewhere between the PALS and the photoisomerization measurements. As discussed in the main text, the r_{tot} distribution obtained from the total cone is larger due to the FVE shape fluctuations that cause spatial locations on the periphery FVE to become accessible, while other locations become inaccessible. The ROAM results then suggest a possible explanation to the discrepancy between the PALS and photoisomerization methods. The PALS measurement is sensitive to the instantaneous FVE size, while the photoisomerization is sensitive to the largest spatial extent available through relatively short time structural relaxation of the polymer. The total cone angle determination of the maximum volume of accessible regions includes regions that are not all simultaneously accessible. For photoisomerization to occur, moieties in different parts of a molecule must be able to move at the same time, requiring even larger FVEs than reported by the ROAM total cone angle size distribution.

1-2 Transition and the Vibrational Stark Effect

Except for the negligibly perturbative differences between the ground and first excited vibrational states of the probe molecule and the anharmonic shift in the emission frequency, both transitions (0-1 transition and 1-2 transition) should yield the same spectroscopic information on the probe molecule dynamics. In particular, we would expect that measurements at the same frequencies relative to the band centers of the 0-1 band and the 1-2 band should yield the same results if the transition frequencies are determined principally by a vibrational Stark effect. The calculated wobbling-in-a-cone

parameters for the two transitions are shown in Fig. S5. Except for moderate differences in the relative amplitudes of the inertial cone θ_0 (which could arise in part from imperfect short-time heat subtraction or non-resonant effects that appear near $t = 0$), the cumulative cone angles match extremely closely. In other words, obtaining the frequency dependent anisotropies on the red side of the 0-1 transition yields the same result as the red side of the 1-2 transition, and the blue side of the 0-1 transition has the same anisotropy as the blue side of the 1-2 transition. Therefore, the orientational dynamics measured starting with the probes in the ground vibrational state and starting in the first excited vibrational are the same.

As shown in the main text, the frequency dependent cone angles and orientational dynamics obtained from the anisotropy decays, $r(t)$, depend on different microscopic structures of the PMMA polymer (see Figs. 1 and 2). Each absorption frequency across the inhomogeneously broadened absorption line is associated with subensembles of probe molecules that reside in structurally very similar environments. Generally, vibrational Stark effect experiments are conducted with linear spectroscopy, so only the 0-1 transition is observed. An important question is whether the Stark effect mechanism is consistent with observing the same site selectivity in the 0-1 and 1-2 transitions. That is, does the Stark effect produce the same frequency dependent site selection in the 0-1 and 1-2 transitions?

Here we show that theory predicts that the Stark effect should produce the same results when observing the 0-1 and 1-2 transitions. The vibrational Stark effect potential can be written compactly to second order in the electric field as follows (16):

$$V = V_0 + \begin{bmatrix} 1 & F & F^2 \end{bmatrix} \begin{bmatrix} 0 & k/2 & \nu_3 & \nu_4 \\ -q & \nu_2' & \nu_3' & 0 \\ \nu_1'' & \nu_2'' & 0 & 0 \end{bmatrix} \begin{bmatrix} x \\ x^2 \\ x^3 \\ x^4 \end{bmatrix} \tag{S3}$$

Where x is the vibrational coordinate, k is the harmonic force constant, q is the effective electric charge of the oscillator, the ν terms are the anharmonic terms of the vibrational potential, ν' terms are the first order Stark effect parameters, and the ν'' terms are the second order Stark effect terms. Finding the energy eigenvalues using standard perturbation theory to second order in x and x^3 and first order in x^4 gives

$$E_n = \left(n+1/2\right)\hbar\omega\left(1-3\frac{BC}{K^2}\right)-\left(30n^2+30n+11\right)\frac{\left(\hbar\omega C\right)^2}{\left(8K\right)^3} \\ -\frac{B^2}{2K}+\frac{3}{2}\left(n^2+n+1/2\right)v_4\left(\frac{\hbar\omega}{K}\right)^2 \quad \text{(S4)}$$

with $B=-qF+v''F^2$, $K=k+2v_2'F+2v_2''F^2$, $C=v_3+v_3'F$, $\omega=\sqrt{K/m}$ and m is the reduced mass of the nitrile mode.

From our Onsager model, we can determine the values of k (18.54 aJ/Å^2) and q (–0.07 aC) for PhSeCN, and from the pump-probe experiment we obtain the value of the anharmonicity, which arises primarily from v_3 (–20.37 aJ/Å^3). The values of the other terms can be estimated by using the parameters determined for 4-chlorobenzonitrile by Stark spectroscopy (16). The purpose of this calculation is principally to show the overall trend of the potential energy levels as a function of field strength, as opposed to obtaining precise numbers.

Plotting the results of Eq. S4 for the first three vibrational energy levels (Fig. S6A) shows that over the range of electric field strengths that are likely to occur in molecular solvents, the vibrational states' energies are monotonic in the field strength. This means that the lower energy side of the vibrational ground state and the lower energy side of the vibrationally excited states correspond to the same field strengths. Fig. S6B shows the 0-1 (black curve) and the 1-2 (red curve) transition frequencies as a function of field strength. The two curves are shifted by the vibrational anharmonicity, but otherwise they are nearly the same. These curves show that a frequency in the 0-1 transition that selects a subensemble of structural sites that has a particular anisotropy decay and therefore associated FVE size (short and long times), is the same at the equivalent 1-2 frequency, which only differs by the vibrational anisotropy.

Effect of the Electric Field on Cone Angles

The main text demonstrated that the calculated electric fields are not strong enough to account for the observed ordering measured by the pump-probe experiment. However, it is still valid to consider if the presence field substantially changes the size of the hard cones necessary to explain the experimental data.

To examine the impact of the field on the cone angles, we can consider the special case of the hard cone and electric field being aligned along the same axis. This special case will greatly simplify the analysis as the potential energy of the dipole is then rotationally symmetric:

$$V(\theta) = \begin{cases} -V_0 \cos\theta & \theta \le \alpha \\ \infty & \theta > \alpha \end{cases} \tag{S5}$$

where $V_0 = \mu_0 F$ for static dipole moment μ_0 and electric field magnitude F. The wobbling-in-a-cone half angle is represented by α. The calculation of the order parameter for the second Legendre polynomial is then (17):

$$S = \left\langle P_2(\cos\theta) \right\rangle = \frac{\int_0^{2\pi} d\phi \int_0^{\pi} d\theta \sin(\theta) \exp\left(-\beta V(\theta)\right) P_2(\cos\theta)}{\int_0^{2\pi} d\phi \int_0^{\pi} d\theta \sin(\theta) \exp\left(-\beta V(\theta)\right)}, \tag{S6}$$

where $\beta = kT$ for Boltzmann constant k and temperature T. Eq. S6 can be solved analytically using Eq. S5:

$$S = \frac{x^2 + 3x + 3}{x^2} - \frac{3e^x \left(\cos(\alpha) - 1\right)\left(x\cos(\alpha) + x + 2\right)}{2x\left(e^{x\cos\alpha} - e^x\right)}, x = \beta V_0 . \tag{S7}$$

Eq. S7 can be shown to go to the electric field limit (Eq. 8) when $\alpha = \pi$ and go to the wobbling-in-the-cone limit (Eq. 5) as x goes to zero.

The experimentally determined order parameters and field strengths can be placed into Eq. S7 to allow for the calculation of the modified cone angles α. The resulting calculated cone angles α are compared to the wobbling-in-a-cone half angles θ in Table S4. The measured angle changes by less than a degree in the case of the total cone angle, and by even less for the θ_{0+1} cone angle. This shows that the presence of electric fields on the order of those measured using the vibrational Stark effect does not invalidate the wobbling-in-a-cone model.

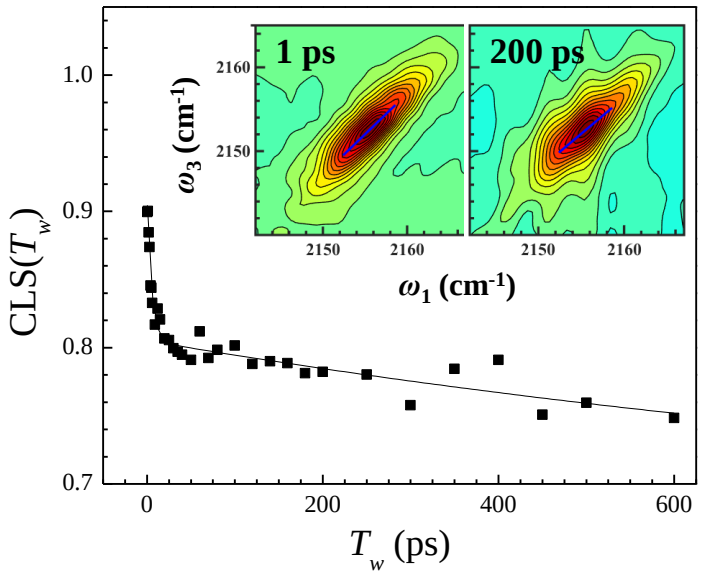

Fig. S1. CLS decay obtained from 2D IR spectroscopy for the entire experimental time scale. The decay shows that the transition frequency of the CN stretch of PhSeCN remains highly correlated during the IR experiments, i.e., different frequencies in the absorption line remain distinct. Inset: Anisotropic 2D spectra of PhSeCN in PMMA at short (T_w = 1) and long (T_w = 200) waiting times. Elongated shapes indicate high correlation in the transition frequency between T_w = 0 and the given T_w.

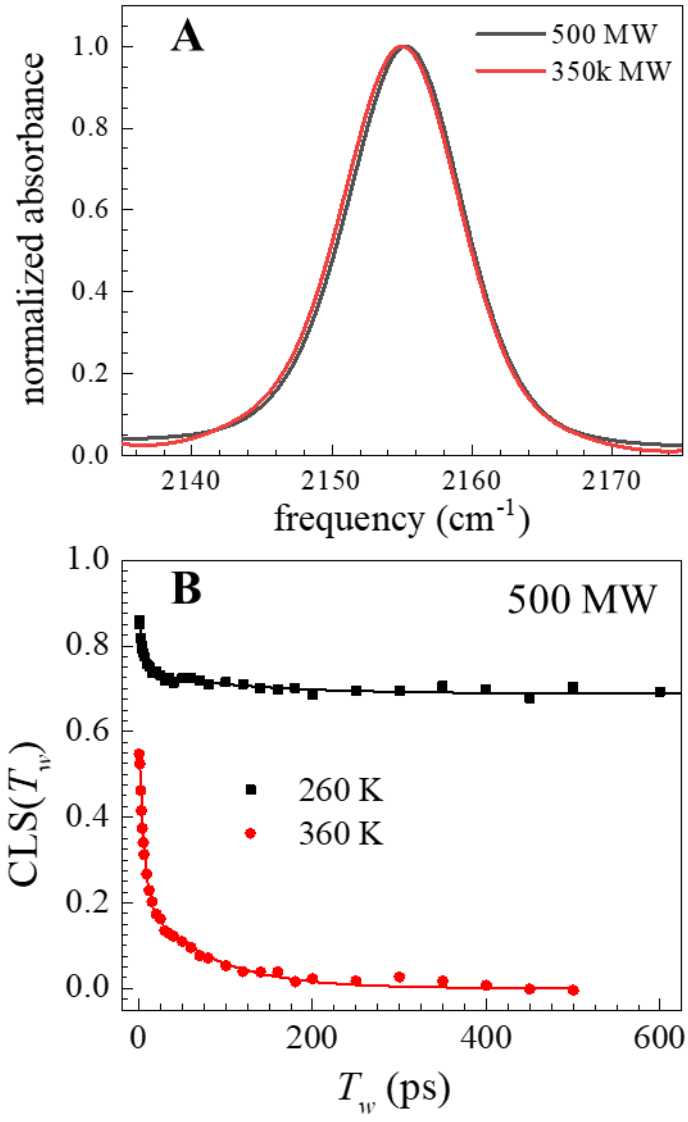

Fig. S2. Spectrum and CLS decay of PhSeCN in the low MW PMMA. **A.** FT-IR spectrum of PhSeCN in low MW PMMA (black curve) vs. the spectrum of PhSeCN in high MW PMMA (red curve). The similarity shows that the PhSeCN is in a similar chemical environment. **B.** CLS decays for the low MW PMMA oligomer at both temperatures. At low temperature the decay is approximately as correlated as the high MW PMMA data. At high temperatures the frequencies completely randomize on the experimental time scale, which is consistent with seeing minimal frequency dependence in the pump-probe anisotropies.

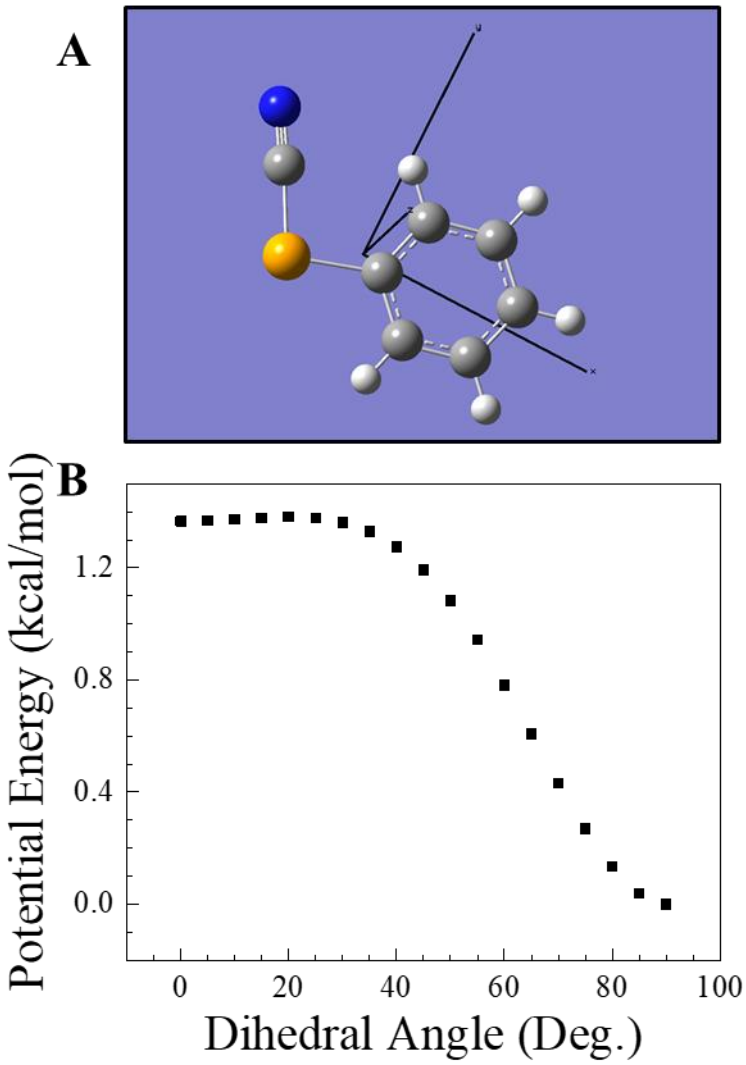

Fig. S3. Results of DFT calculations on PhSeCN. **A.** Center of mass (found at the intersection of axes) of PhSeCN. **B.** Potential energy surface for rotation around the C-Se bond between the SeCN and phenyl group. The maximum is about 1.38 kcal/mol.

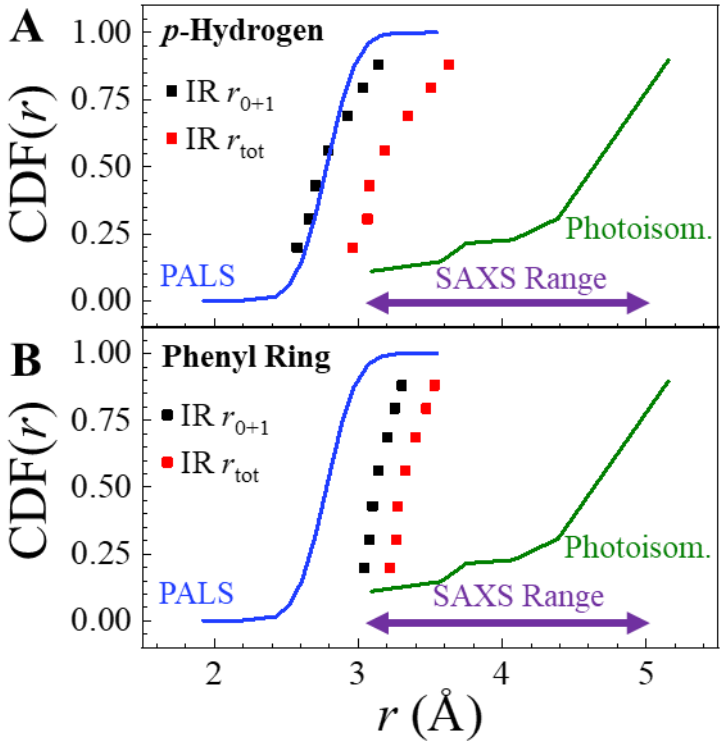

Fig. S4. Comparison of ROAM results to literature results. **A.** Comparison of the cumulative distribution functions (CDF) of radii r_{0+1} and r_{tot} for PhSeCN in PMMA using the *p*-hydrogen ROAM model (this work) and the literature free volume radii cumulative distribution measured by the PALS (18), the photoisomerization method (11), and SAXS (15). The r_{0+1} distribution is very similar to the PALS distribution. The photoisomerization measurements are much larger than what was found with ROAM and PALS. **B.** Comparison of the CDF of the phenyl ring ROAM model to literature distributions.

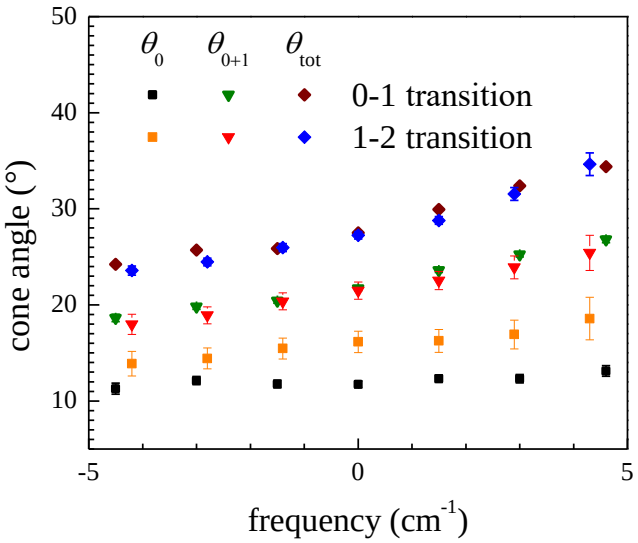

Fig. S5. Cone angles for the 1-2 transition anisotropy decays compared to those for the 0-1 transition. On the horizontal axis, 0 is the center frequency of each transition. θ_{0+1} and θ_{tot} are essentially identical for the two transitions, showing the two transitions report on the same frequency dependent dynamics. The small differences in θ_0 (the ultrafast inertial component) could arise from imperfect heat subtraction at short time or non-resonant effects.

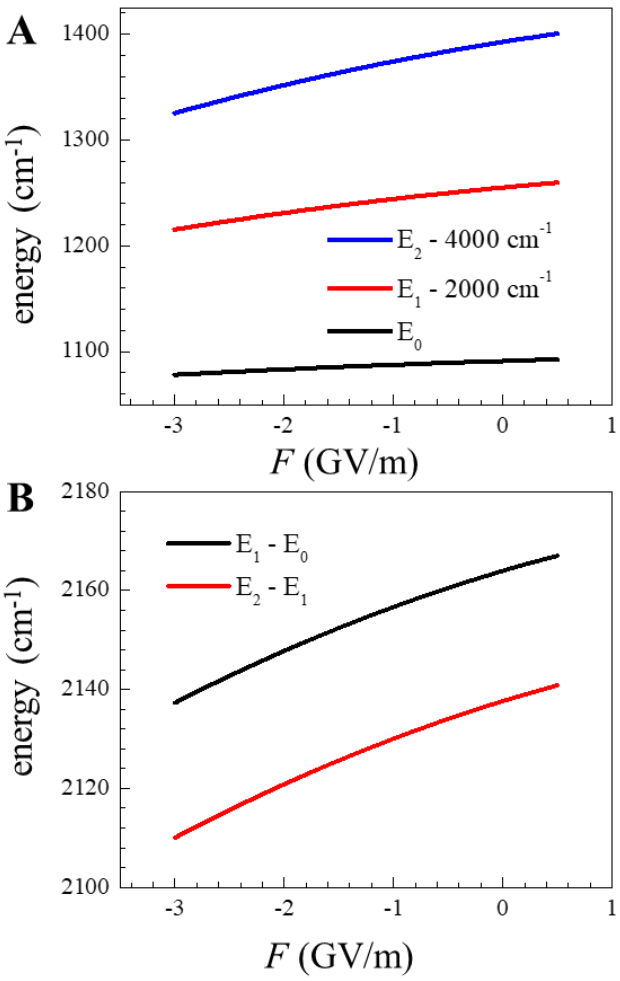

Fig. S6. Energy levels for a quantum harmonic oscillator with the vibrational Stark effect. **A.** Vibrational energy levels as a function of electric field strength (see SI). Each energy level is monotonic in field strength. The levels are offset for clarity. **B.** Vibrational transition energies for the 0-1 and 1-2 transitions (see Fig. 1B) as a function of field strength. The transition energies are also monotonic in field strength and essentially the same as a function of field strength except for the vibrational anharmonic shift.

Table S1. Fit Parameters to the Wobbling-in-a-Cone Model for High Mw PMMA at 297 K.

Angles θ_i relate to order parameters S_i by Eq. 5.

frequency (cm^{-1})	θ_0 (°)	θ_1 (°)	τ_1 (ps)	θ_2 (°)	τ_2 (ps)	θ_{0+1} (°)	θ_{tot} (°)
2159.3	13.1 ± 0.6	23.5 ± 0.2	9.8 ± 0.5	22.2 ± 0.2	266 ± 20	26.8 ± 0.3	34.4 ± 0.2
2157.7	12.3 ± 0.4	22.2 ± 0.2	9.5 ± 0.4	20.8 ± 0.2	261 ± 16	25.2 ± 0.3	32.4 ± 0.1
2156.2	12.3 ± 0.4	20.3 ± 0.2	9.4 ± 0.4	18.8 ± 0.2	239 ± 15	23.6 ± 0.2	29.9 ± 0.1
2154.7	11.7 ± 0.4	18.4 ± 0.2	8.1 ± 0.4	17.2 ± 0.2	180 ± 10	21.7 ± 0.2	27.5 ± 0.1
2153.2	11.8 ± 0.4	16.8 ± 0.2	7.8 ± 0.5	16.1 ± 0.2	185 ± 13	20.4 ± 0.3	25.9 ± 0.1
2151.7	12.1 ± 0.4	15.8 ± 0.2	8.0 ± 0.5	16.6 ± 0.2	285 ± 22	19.8 ± 0.3	25.7 ± 0.1
2150.2	11.3 ± 0.6	14.9 ± 0.3	6.2 ± 0.7	15.7 ± 0.2	233 ± 24	18.6 ± 0.4	24.2 ± 0.2

Table S2. Fit Parameters to the Wobbling-in-a-Cone Model for Low Mw PMMA at 260 K.

Angles θ_i relate to order parameters S_i by Eq. 5. Radii r_i determined with the *p*-hydrogen model.

frequency (cm^{-1})	θ_0 (°)	θ_1 (°)	τ_1 (ps)	θ_2 (°)	τ_2 (ps)	θ_{0+1} (°)	θ_{tot} (°)
2159.3	5 ± 4	20.2 ± 0.7	10 ± 2	23.7 ± 0.5	222 ± 32	21 ± 1	31.3 ± 0.3
2157.7	6 ± 2	19.2 ± 0.5	11 ± 1	23.3 ± 0.3	255 ± 27	20.2 ± 0.7	30.6 ± 0.3
2156.2	9 ± 1	17.7 ± 0.4	12 ± 1	23.1 ± 0.2	295 ± 23	19.7 ± 0.5	30 ± 0.2
2154.7	9.1 ± 0.8	16.5 ± 0.3	13 ± 1	22.2 ± 0.2	292 ± 19	18.8 ± 0.4	28.8 ± 0.2
2153.2	10.3 ± 0.7	14.7 ± 0.3	13 ± 1	21.5 ± 0.2	293 ± 18	17.9 ± 0.4	27.8 ± 0.2
2151.7	11.4 ± 0.7	12.7 ± 0.4	13 ± 2	20.5 ± 0.2	279 ± 20	17.1 ± 0.5	26.5 ± 0.2
2150.2	12.2 ± 0.8	10.8 ± 0.7	11 ± 3	20 ± 0.3	261 ± 25	16.3 ± 0.7	25.6 ± 0.2

frequency (cm^{-1})	r_{0+1} (Å)	r_{tot} (Å)
2159.3	2.73	3.43
2157.7	2.69	3.39
2156.2	2.65	3.35
2154.7	2.59	3.27
2153.2	2.52	3.20
2151.7	2.46	3.12
2150.2	2.41	3.06

Table S3. Fit Parameters to the Wobbling-in-a-Cone Model for Low Mw PMMA at 360 K.

Data fit to Eq. S1. Angles θ_i relate to order parameters S_i by Eq. 5. Radii r_i determined with the *p*-hydrogen model.

frequency (cm^{-1})	θ_0 (°)	θ_1 (°)	τ_1 (ps)	θ_2 (°)	τ_2 (ps)	θ_{0+1} (°)	θ_{tot} (°)	τ_{or} (ps)
2159.3	22 ± 4	40 ± 2	4.8 ± 1	54 ± 4	34 ± 10	45 ± 4	66 ± 3	380 ± 117
2157.7	22 ± 3	38 ± 2	5.2 ± 0.7	53 ± 3	38 ± 9	43 ± 3	65 ± 3	267 ± 62
2156.2	22 ± 3	37 ± 2	5.7 ± 0.8	51 ± 3	41 ± 10	42 ± 3	63 ± 3	212 ± 43
2154.7	21 ± 5	34 ± 2	5.5 ± 1	45 ± 4	36 ± 13	39 ± 4	58 ± 4	133 ± 26
2153.2	21 ± 9	31 ± 5	5 ± 2	39 ± 6	31 ± 23	37 ± 8	52 ± 6	96 ± 21
2151.7	21 ± 11	29 ± 6	5 ± 2	38 ± 7	31 ± 25	36 ± 10	50 ± 7	96 ± 24

frequency (cm^{-1})	r_{0+1} (Å)	r_{tot} (Å)
2159.3	4.22	5.13
2157.7	4.16	5.10
2156.2	4.08	5.03
2154.7	3.92	4.83
2153.2	3.79	4.59
2151.7	3.71	4.52

Table S4. Comparing cone angles with and without inclusion of dipolar ordering by the local electric fields

F determined by Eq. 6 in main text. θ_i is the same as in Table S1. α_i derived from Eq. S7.

Freq. (cm^{-1})	*F* (GV/m)	θ_{0+1} (°)	α_{0+1} (°)	θ_{tot} (°)	α_{tot} (°)
2159.3	-0.36	26.8	27.1	34.4	35.0
2157.7	-0.49	25.2	25.6	32.4	33.1
2156.2	-0.61	23.6	24.0	29.9	30.7
2154.7	-0.73	21.7	22.0	27.5	28.2
2153.2	-0.85	20.4	20.8	25.9	26.5
2151.7	-0.98	19.8	20.2	25.7	26.5
2150.2	-1.10	18.6	19.0	24.2	24.9

SI References

1. S. Park, K. Kwak, M. D. Fayer, Ultrafast 2D-IR vibrational echo spectroscopy: A probe of molecular dynamics. *Laser Phys. Lett.* **4**, 704-718 (2007).
2. P. Hamm, M. Zanni, *Concepts and methods of 2D infrared spectroscopy* (Cambridge University Press, 2011).
3. S. K. Karthick Kumar, A. Tamimi, M. D. Fayer, Comparisons of 2D IR measured spectral diffusion in rotating frames using pulse shaping and in the stationary frame using the standard method. *J. Chem. Phys.* **137**, 184201 (2012).
4. K. Kwak, S. Park, I. J. Finkelstein, M. D. Fayer, Frequency-frequency correlation functions and apodization in two-dimensional infrared vibrational echo spectroscopy: a new approach. *J. Chem. Phys.* **127**, 124503 (2007).
5. K. Kwak, D. E. Rosenfeld, M. D. Fayer, Taking apart the two-dimensional infrared vibrational echo spectra: more information and elimination of distortions. *J. Chem. Phys.* **128**, 204505 (2008).
6. P. L. Kramer, J. Nishida, C. H. Giammanco, A. Tamimi, M. D. Fayer, Observation and theory of reorientation-induced spectral diffusion in polarization-selective 2D IR spectroscopy. *J. Chem. Phys.* **142**, 184505 (2015).
7. P. L. Kramer, J. Nishida, M. D. Fayer, Separation of experimental 2D IR frequency-frequency correlation functions into structural and reorientation-induced contributions. *J. Chem. Phys.* **143**, 124505 (2015).
8. H. S. Tan, I. R. Piletic, M. D. Fayer, Orientational dynamics of water confined on a nanometer length scale in reverse micelles. *J. Chem. Phys.* **122**, 174501 (2005).
9. G. Lipari, A. Szabo, Effect of librational motion on fluorescence depolarization and nuclear magnetic resonance relaxation in macromolecules and membranes. *Biophys. J.* **30**, 489-506 (1980).
10. J. G. Victor, J. M. Torkelson, On Measuring the Distribution of Local Free Volume in Glassy Polymers by Photochromic and Fluorescence Techniques. *Macromolecules* **20**, 2241-2250 (1987).
11. J. S. Royal, J. G. Victor, J. M. Torkelson, Photochromic and Fluorescent Probe Studies in Glassy Polymer Matrices. 4. Effects of Physical Aging on Poly(methyl

methacrylate) As Sensed by a Size Distribution of Photochromic Probes. *Macromolecules* **25**, 729-734 (1992).

12. J. Liu, Q. Deng, Y. C. Jean, Free-Volume Distributions of Polystyrene Probed by Positron Annihilation: Comparison with Free-Volume Theories. *Macromolecules* **26**, 7149-7155 (1993).
13. Y. P. Yampolskii, Methods for investigation of the free volume in polymers. *Russ. Chem. Rev.* **76**, 59-78 (2007).
14. Z. X. Low, P. M. Budd, N. B. McKeown, D. A. Patterson, Gas Permeation Properties, Physical Aging, and Its Mitigation in High Free Volume Glassy Polymers. *Chem. Rev.* **118**, 5871-5911 (2018).
15. L. David *et al.*, Density fluctuations in amorphous systems: SAXS and PALS results. *J. Non-Cryst. Solids* **235-237**, 383-387 (1998).
16. S. S. Andrews, S. G. Boxer, Vibrational Stark effects of nitriles II. Physical origins of Stark effects from experiment and perturbation models. *J. Phys. Chem. A* **106**, 469-477 (2002).
17. S. Stallinga, Effect of rotational diffusion in an orientational potential well on the point spread function of electric dipole emitters. *J. Opt. Soc. Am. A* **32**, 213 (2015).
18. C. Wästlund, F. H. J. Maurer, Positron lifetime distributions and free volume parameters of PEO/PMMA blends determined with the maximum entropy method. *Macromolecules* **30**, 5870-5876 (1997).